

Anchored Ligands Facilitate Efficient B-Site Doping in Metal Halide Perovskites

Zhenyu Yang,^{†,‡,¶,||} Mingyang Wei,^{†,‡} Oleksandr Voznyy,[†] Petar Todorovic,[†] Mengxia Liu,[†] Rafael Quintero-Bermudez,[†] Peining Chen,[†] James Z. Fan,[†] Andrew H. Proppe,^{†,‡} Li Na Quan,[†] Grant Walters,[†] Hairen Tan,[†] Je-Wei Chang,[§] U-Ser Jeng,^{§,||} Shana O. Kelley,^{‡,⊥} and Edward H. Sargent^{*,†}

[†]Department of Electrical and Computer Engineering, University of Toronto, 10 King's College Road, Toronto, Ontario, Canada, M5S 3G4

[‡]Department of Chemistry, University of Toronto, 80 St. George Street, Toronto, Ontario, Canada, M5S 3H6

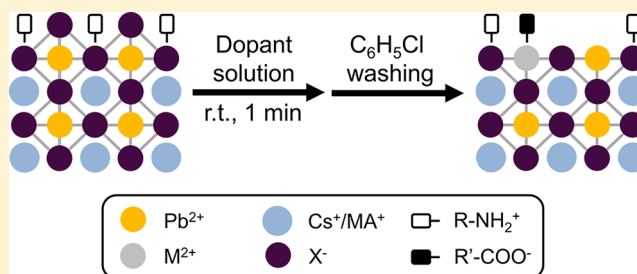
[§]Department of Chemical Engineering, National Tsing Hua University, Hsinchu 300, Taiwan

^{||}National Synchrotron Radiation Research Center, Hsinchu Science Park, Hsinchu 300, Taiwan

[⊥]Department of Pharmaceutical Sciences, Leslie Dan Faculty of Pharmacy, University of Toronto, Toronto, Ontario, Canada, M5S 3M2

Supporting Information

ABSTRACT: Metal halide perovskites exhibit outstanding optoelectronic properties: superior charge carrier mobilities, low densities of deep trap states, high photoluminescence quantum yield, and wide color tunability. The introduction of dopant ions provides pathways to manipulate the electronic and chemical features of perovskites. In metal halide perovskites ABX_3 , where A is a monovalent cation (e.g., methylammonium (MA^+), Cs^+), B is the divalent metal ion(s) (e.g., Pb^{2+} , Sn^{2+}), and X is the halide group (e.g., Cl^- , Br^- , or I^-), the isoivalent exchange of A- and X-site ions has been widely accomplished; in contrast, strategies to exchange B-site cations are underexamined. The activation energies for vacancy-mediated diffusion of B-site cations are much higher than those for A- and X-sites, leading to slow doping processes and low doping ratios. Herein we demonstrate a new method that exchanges B-site cations in perovskites. We design a series of metal carboxylate solutions that anchor on the perovskite surface, allowing fast and efficient doping of B-sites with both homovalent and heterovalent cations (e.g., Sn^{2+} , Zn^{2+} , Bi^{3+}) at room temperature. The doping process in the reduced-dimensional perovskites is complete within 1 min, whereas a similar reaction only leads to the surface attachment of dopant ions in three-dimensional structures. We offer a model based on ammonium extraction and surface ion-pair substitution.



1. INTRODUCTION

The incorporation of impurity elements into semiconductors is among the foundations of solid-state chemistry for electronics. The electronic levels of pristine materials can be tailored by control over the class and concentration of foreign atoms in an otherwise pure and regular crystal lattice. Doping adds a degree of freedom in the preparation of semiconductor materials with modified optical and electronic properties including in photovoltaics, transistors, light-emitting diodes, photodetectors, nonlinear optics, and catalysts.^{1–6}

The doping of semiconductors in various forms—bulk crystals, thin films, nanocrystals—has been explored and applied in both research and mass production. Doping of a semiconductor (including group IV, II–VI, III–V, and I–III–VI materials) is achieved via direct crystal growth of predesigned cation/anion mixtures or alternatively using postsynthetic ion exchange/diffusion.^{7,8}

Metal halide perovskites hold advantages over traditional semiconductors in the simplicity of solution- or gas-phase fabrication, their low defect densities, and their tuning via compositionally dependent optoelectronic properties. The scaffold enables the insertion of bulky organic cations to enhance carrier confinement and structural stability, of greater interest in both light emission and photovoltaics.^{9–12}

In metal halide perovskites, the Goldschmidt tolerance factor has been widely used as the empirical index to predict stability of the crystal structure. When the tolerance factor is within the allowable regime,¹³ replacement of an anion or cation becomes possible. A wide range of three-dimensional (3D) perovskites, and also RD perovskites (a.k.a. 2D and 2.5D), have been doped according to this principle. Methods

Received: March 8, 2019

Published: May 4, 2019

similar to those used in conventional semiconductors have been used to prepare doped perovskites with mixed cations or anions.^{14–16} While the incorporation of heterovalent ions is possible,^{17–19} most doping processes for perovskites favor isovalent elements to maintain charge balance and low crystal distortion.^{20,21}

Postsynthetic processes enable efficient dopant incorporation and can maintain the morphology of the materials under mild conditions. Through the interaction of an undoped semiconductor with a dopant source (e.g., soaking in a solution that contains dopant element), the diffusion of the dopants and chemical reactions initiate and propagate the doping process.²² Driven by external motive forces such as light, electric field, and the ion concentration gradient, ionic exchange offers efficient doping and fine-tuning of the A- and X-site compositions in perovskites.^{23,24}

Unfortunately, the energy required to form a B-site vacancy is much larger than that needed to form A- and X-site vacancies. For this reason, the A-/X-site approach implemented on the B-site achieves slow exchange (e.g., it can take multiple days²⁵), and only isovalent element exchange has been reported to date.^{25–27} A general method to produce efficient B-site doping in metal halide perovskites has yet to be demonstrated.

Here we develop the surface chemistry to perform facile and rapid B-site exchange on perovskites. Noting efficient ligand–ligand interaction at the surface of nanomaterials,²⁸ we developed a B-site doping strategy that uses a metal carboxylate to anchor the dopant elements on perovskites. This facilitates B-site vacancy formation and enables impurity cation diffusion that yields homogeneously doped reduced-dimensional perovskite materials. The doping process relies on the presence of bulky organic ions: as a key step in the doping process, metal carboxylate interacts with organic ammonium and halide groups, cleaving the PbX_4^{2-} octahedron and thus allowing the exchange between targeted dopants and Pb^{2+} . We found that when the crystal tolerance factor allows it, the B-site exchange can proceed at room temperature within 1 min. We investigated the ensuing crystal change (e.g., expansion or shrinkage) using high-energy X-ray diffraction (HE-XRD) and grazing-incidence wide-angle X-ray scattering (GIWAXS). We achieve a highest doping rate of the heterovalent cation of 14% for reduced-dimensional perovskite films, 40 times higher than achieved using previously reported perovskite doping processes.¹⁷

2. EXPERIMENTAL SECTION

Materials. All chemicals used are commercially available and were used without any additional purification steps: lead(II) iodide (PbI_2 , Alfa Aesar, 99.999%, ultradry), lead(II) bromide (PbBr_2 , Alfa Aesar, 99.999%, ultradry), methylammonium iodide (MAI, Dyesol Inc., 99.9%), methylammonium bromide (MABr, Dyesol Inc., 99.9%) phenylethylammonium bromide (PEABr, Dyesol Inc., 99.9%), *n*-hexylammonium bromide, $\text{C}_6\text{H}_{13}\text{NH}_3\text{Br}$ (HABr, Dyesol Inc.), cesium bromide (CsBr , Sigma-Aldrich, 99.999%), bismuth 2-ethylhexanoate ($\text{Bi}(\text{Oct})_3$, Alfa Aesar, 96.2%), tin(II) 2-ethylhexanoate ($\text{Sn}(\text{Oct})_2$, Sigma-Aldrich, 92.5–100.0%), zinc 2-ethylhexanoate ($\text{Zn}(\text{Oct})_2$, Alfa Aesar, ca. 80% in mineral spirits (17–19% Zn)), lithium 2-ethylhexanoate (LiOct , Alfa Aesar, 99%), chlorobenzene (anhydrous, Caledon), toluene (anhydrous, Caledon), *N,N*-dimethylformamide (DMF, Sigma-Aldrich, 99.8%), methyl sulfoxide (DMSO, Sigma-Aldrich, $\geq 99\%$), chloroform (anhydrous, Sigma-Aldrich), ethyl acetate (anhydrous, Sigma-Aldrich, 99.8%), γ -butyrolactone (GBL, Sigma-Aldrich, $\geq 99\%$).

Synthesis of Bromide Perovskite Nanoplatelets. Colloidal perovskite nanoplatelets ($n = 2$) were synthesized from solution following a variation of published methods.^{29,30} PbBr_2 , MABr, and HABr were added to DMF to form a precursor solution. The concentration of PbBr_2 was held at 0.06 M, while the ratios of the organic cation components were varied to control the thickness and phase purity of the nanoplatelets. The concentration of MABr and HABr was 0.03 and 0.06 M, respectively. A 20 μL amount of the precursor solution was added dropwise into 1 mL of chlorobenzene while stirring vigorously. As the perovskite precursors are introduced to the antisolvent, they crystallize immediately as colloidal nanoplatelets capped by the large organic cations present in the precursor solution. A color change is observed from the addition of the precursor solution, and bright photoluminescence can be observed when the nanoplatelets are held under 365 nm UV light.

Preparation of Reduced-Dimensional Perovskite Films. For the synthesis of $(\text{PEA})_2\text{Cs}_4\text{Pb}_3\text{Br}_{16}$ and $(\text{PEA})_2\text{MA}_4\text{Pb}_3\text{Br}_{16}$ perovskites (i.e., $n = 5$), all precursors, including PbBr_2 (183.5 mg, 0.50 mmol), CsBr (79.2 mg, 0.37 mmol) or MABr (41.4 mg, 0.37 mmol), and PEABr (50.5 mg, 0.25 mmol), were completely dissolved in 1.0 mL of DMSO at room temperature, equipped with a small Teflon-coated stir bar. The solution was then spin-cast onto a clean glass substrate with a two-step spin-casting setup: in the first step, 70 μL of the precursor solution was dropped onto the substrate and immediately spin-cast with a spin rate of 1000 rpm for 10 s; then the spin rate increased to 5000 rpm for 60 s. During the second step (i.e., 5000 rpm) of the spin-cast process (30 s remaining), 100 μL of chloroform as antisolvent was dropped onto the substrate. The film was further annealed at 90 °C for 5 min under a nitrogen atmosphere. After cooling to room temperature, samples were stored in a nitrogen-filled glovebox for further use.

Preparation of MAPbI_3 Perovskite Films. The MAPbI_3 precursor solutions (1.4 M) were prepared by the dissolution of an equal amount of MAI and PbI_2 precursors in a mixed solvent of DMF and DMSO with a volume ratio of 1:1. The perovskite films were deposited onto clean glass substrates with two-step spin-coating procedures: in the first step, 80 μL of the mixed solution was drop cast onto the substrate, which was then immediately spun at 200 rpm for 10 s with an acceleration of 200 rpm/s; in the second step, the spin speed was increased to 4000 rpm for 30 s with a ramp-up of 1000 rpm/s. A 100 μL amount of chlorobenzene was dropped on the spinning substrate during the second spin-coating step at 20 s before the end of the procedure. The sample was then immediately transferred on a hot plate and heated at 100 °C for 30 min. After cooling to room temperature, samples were stored in a nitrogen-filled glovebox for further use.

Preparation of Dopant Solutions. A 0.5 v/v% amount of dopant solution was prepared by fully dissolving the metal ethylhexanoate (i.e., $\text{Sn}(\text{Oct})_2$, $\text{Bi}(\text{Oct})_3$, $\text{Zn}(\text{Oct})_2$, liquid state) into chlorobenzene under a nitrogen atmosphere. It is important to note that the solubility of LiOct solid in chlorobenzene is limited; the dissolution of LiOct requires prolonged mechanical stirring at 70 °C for 2 h, and the solution was filtered through a 0.2 μm syringe filter to remove undissolved salt. All dopant solution was stored in a nitrogen-filled glovebox for further use.

Solid-State B-Site Exchange of Perovskite Thin Films. In a nitrogen-filled glovebox, 5 mL of the dopant solution was transferred to a 20 mL vial, and a small piece of the perovskite thin film (0.5 in. by 0.5 in.) was immersed into the solution at room temperature. After soaking for 30 s, the perovskite film was taken out, further washed by clean chlorobenzene twice, and dried under a nitrogen atmosphere. Samples were stored in a nitrogen-filled glovebox for further use.

Photoluminescence and Absorption Measurement. Photoluminescence measurements were done with a Horiba Fluorolog time-correlated single photon counting system equipped with UV/vis/NIR photomultiplier tube detectors, dual grating spectrometers, and a monochromatized xenon lamp excitation source. Optical absorption measurements were carried out in a Lambda 950 UV–vis–IR spectrophotometer.

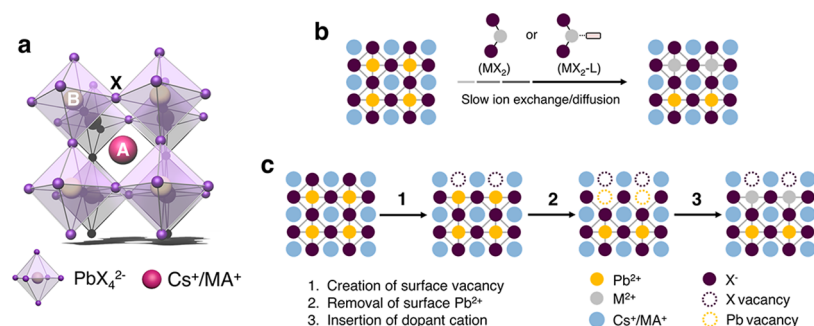


Figure 1. B-site cation exchange strategies. (a) Lead halide perovskite structure. (b) Mechanism in previously reported B-site doping/exchange methods, where the exchange rate is limited by the slow exchange/diffusion of B-site cations provided by dopant halide salts (MX_2) and their organic complexes ($\text{MX}_2\text{-L}$). (c) Proposed new B-site doping mechanism: the creation of surface halide vacancy and removal of surface lead ion using surface ligand anchoring seeks to facilitate rapid B-site doping.

Powder X-ray Diffraction. Powder X-ray diffraction (PXRD) samples were either prepared by spin-coating of solution samples (nanoplatelets) on a glass substrate or used directly (film samples such as reduced-dimensional and MAPbI_3 perovskites). Measurements were taken by using a Rigaku Miniflex 600 diffractometer with a NaI scintillation counter and using monochromatized $\text{Cu K}\alpha$ radiation (1.5406 Å). XRD spectra were scanned between 2θ ranges of 3–50 °C with an integration of 0.5 s.

High-Energy X-ray Diffraction and Pair Distribution Function Analysis. RD and 3D perovskite thin-film samples were made using the above-mentioned spin-coating process. High-energy X-ray diffraction experiments were conducted at the 6-ID-D beamline at APS (Argonne National Laboratory, USA). The energy of the X-ray incident beam was 100.329 keV. The two-dimensional (2D) setup was applied for data collection with a PerkinElmer model 1621 X-ray area detector. The results of the diffraction patterns were calculated using the Fit2D software.

X-ray Photoelectron Spectroscopy (XPS) Measurements. XPS measurements were carried out with the Thermo Scientific K-Alpha XPS system. An Al $\text{K}\alpha$ source with a 400 μm spot size was used for measurements to detect photoelectrons at specific energy ranges to determine the presence of specific elements. Sputter depth profiling was performed with an ion gun at 2 keV to avoid spurious features (e.g., ion beam damage), where each step has a duration of 30 s.

Transient Absorption (TA) Measurements. A regeneratively amplified Yb:KGW laser at a 5 kHz repetition rate (Light Conversion, Pharos) was used to generate femtosecond laser pulses, and a pulse picker was used to lower the frequency to 1 kHz. A portion of the 1030 nm fundamental was sent into an optical bench (Ultrafast, Helios), where it passed through a retroreflector and was then focused into a calcium fluoride crystal, translated at 1 mm/s, to create the white light continuum probe. An optical parametric amplifier (Light Conversion, Orpheus) was used to generate the 375 nm pump pulse by up-conversion of the fundamental wavelength. This was then sent to the optical bench and was chopped at 500 Hz. Both the pump and probe were sent to the sample, with the time delay adjusted by changing the path length of the probe (time resolution ~ 350 fs). The probe pulse was then collected by a CCD after dispersion by a grating spectrograph (Ultrafast). Kinetic traces were fit to the convolution of the instrument response and a sum of exponential decays. Time zero was allowed to vary with wavelength to account for the chirp of the probe.

Inductively Coupled Plasma Optical Emission Spectrometer (ICP-OES) Analysis. Perovskite thin films were completely dissolved in 4% w/w HNO_3 aqueous solution. The solutions were then filtered through 200 μm syringe filters before the characterization. The atomic composition of the sample was determined using an ICP-OES (Agilent Dual-View 720 with CCD for full wavelength coverage between 167 and 785 nm). Standard solutions (0.2, 2, 20, 200, and 1000 ppm) of characterized elements (i.e., Pb, Sn, Bi, Zn, Li) were prepared for calibration. Calibration curves of each element are shown in Figures S5–S7.

Grazing Incidence Wide-Angle X-ray Scattering Measurement. GIWAXS was conducted at the 23A SWAXS beamline of the Taiwan Light source of the National Synchrotron Radiation Research Center, Hsinchu.³¹ With a 10 keV beam, GIWAXS data were collected using a CMOS flat panel detector, C10158DK-3957 ($10 \times 10 \text{ cm}^2$), with a sample-to-detector distance of 180 mm and an incident angle $\alpha = 2.0^\circ$. With the sample plane defined as the x - y plane and the incident X-ray beam in the x - z plane, the scattering vector q is defined by $q_x = 2\pi\lambda^{-1}(\cos\beta\cos\varphi - \cos\alpha)$, $q_y = 2\pi\lambda^{-1}(\cos\beta\sin\varphi)$, and $q_z = 2\pi\lambda^{-1}(\sin\alpha + \sin\beta)$. Here, β is the exit angle and φ is the scattering angle away from the y - z plane, and the in-plane scattering vector $q_r = (q_x^2 + q_y^2)^{1/2}$. The scattering peak positions were calibrated rigorously using the diffraction peaks from powders of Si, Ag-behenate, and LaB_6 .

3. RESULTS AND DISCUSSION

Design of a B-Site Doping Strategy. The efficiency of ion exchange is determined by the activation energy of the corresponding vacancy diffusion since ion exchange within the perovskite is driven principally by vacancy migration. The activation energy for Pb^{2+} migration within the perovskite lattice assisted by a vacancy is 2.2 eV, which is ~ 2.75 and 4 times higher than for the migration of A- and X-site ions in MAPbI_3 , respectively (Figure 1a).³² The large activation energy barrier therefore severely curtails the exchange rate of Pb^{2+} by homovalent and heterovalent dopants through postsynthetic approaches. This is reflected in the reported slow B-site cation exchange occurring at the interface between perovskite and the dopant halide salt and/or the corresponding dopant salt/organic complexes that are dissolved in hydrophobic solution^{25,26,33} (Figure 1b).

Cation exchange inefficiency (with the correspondingly high calculated barrier) arises structurally from the protection of the Pb^{2+} ion by the rigid PbX_4^{2-} octahedral cage and the insolubility of Pb^{2+} in a hydrophobic environment. We reasoned therefore that to create surface halide vacancies, and then to attach bulky ligands, would promote efficient B-site cation exchange (Figure 1c). Inspired by the ligand exchange between carboxylate ions and ammonium passivants on quantum dot surfaces,³⁴ we investigated metal carboxylates as viable exchange promoters.

Reactions on Nanoplatelets. We investigated the efficiency of the ammonium/carboxylate ligand exchange on free-standing perovskite nanoplatelets, on which bulky organic ligands are more readily able to interact with ions in solution. We implemented in situ ligand exchange by adding metal ethylhexanoate (M_xOct_y) salt solution containing predesigned dopant cations (e.g., Sn^{2+} , Bi^{3+} , Zn^{2+} , Li^+) into the

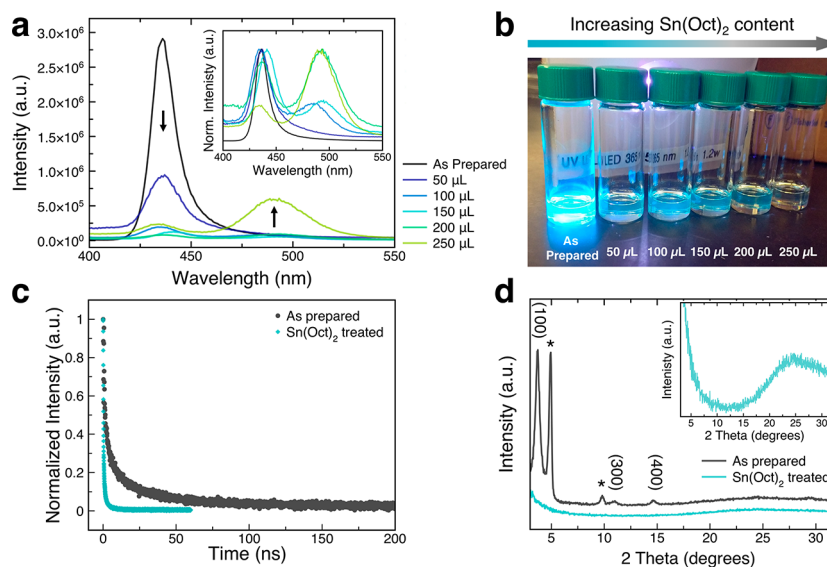


Figure 2. Photoluminescence and crystalline properties of doped nanoplatelets. (a) Photoluminescence (PL) spectra of $n = 2$ perovskite nanoplatelet solutions after mixing with the indicated amount of $\text{Sn}(\text{Oct})_2$ solution (arrows indicate the direction intensity change of two major photoluminescence peaks following the doping treatment). Inset: Normalized PL spectra showing the shift of PL signal after dopant treatment. (b) Corresponding nanoplatelet solutions shown in (a). (c, d) Photoluminescence lifetime decay curves of nanoplatelet solutions and powder X-ray diffraction (PXRD) patterns of nanoplatelet powders before and after $\text{Sn}(\text{Oct})_2$ solution treatment. Signals originating from $n = 1$ perovskite structures are denoted using asterisks (*). Inset: Zoom-in PXRD pattern showing the amorphous structure of dopant-treated nanoplatelet sample.

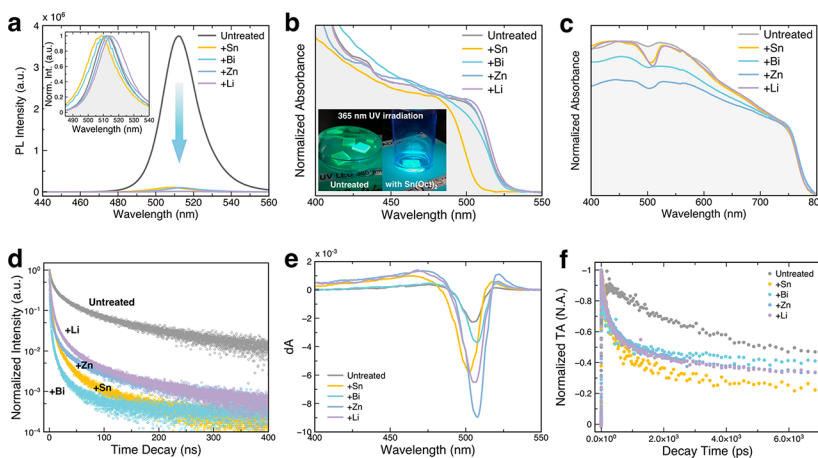


Figure 3. Photophysical properties of doped perovskite thin films. (a) Photoluminescence spectra and (b) absorption spectra of RD perovskites ($(\text{PEA})_2\text{Cs}_4\text{Pb}_5\text{Br}_{16}$) before and after various dopant treatments. Inset: Pictures of 365 nm irradiated RD perovskite samples before treatment and immersed in the solution of $\text{Sn}(\text{Oct})_2$. (c) Absorption spectra of 3D perovskites (MAPbI_3) before and after dopant treatments. (d) Photoluminescence lifetime decay results of the corresponding RD perovskites shown in (b). (e) Transient absorption spectra of doped and undoped RD perovskites at 5 ps after pump excitation. (f) Transient absorption spectral dynamics for different RD perovskites probe wavelengths corresponding to their respective ground-state bleach features. Accelerated quenching of the bleach signal is observed when dopants are introduced.

$(\text{PEA})_2\text{Cs}_4\text{Pb}_5\text{Br}_{16}$ nanoplatelet solution and then isolated and purified the product (Experimental Section).

Prior to ligand exchange, strong blue photoluminescence (PL) at 436 nm indicates well-defined $n = 2$ perovskite nanoplatelets (Figure 2a and b). The photoexcited state lifetime decay values τ_1 and τ_2 of the original nanoplatelets are 1.8 and 23 ns, respectively (Figure 2c); these are similar to previously reported values for $n = 2$ perovskites and are assigned to recombination within the layered perovskite quantum well.³⁰ When a trace amount of $\text{Sn}(\text{Oct})_2$ (0.03 M in chlorobenzene) is added and mixed for less than 1 min, the PL intensity is substantially diminished. A new, smaller and broader PL contribution grows in the 480 nm range and the intensity becomes stronger following the increase of $\text{Sn}(\text{Oct})_2$

content, whereas the absorption peak of the nanoplatelets shifts by only 2 nm following the reaction. The PL change is observed only when Sn^{2+} is present. The corresponding lifetime decay values are much smaller than those from untreated nanoplatelets ($\tau_1 = 0.21$ ns, $\tau_2 = 1.8$ ns, Figure 2c).

These perovskite nanoplatelets become unstable following the $\text{Sn}(\text{Oct})_2$ treatment. The original nanoplatelets show well-defined $n = 2$ perovskite crystalline signals under powder X-ray diffraction (XRD, Figure 2d). However, no crystalline feature of the $\text{Sn}(\text{Oct})_2$ -treated sample is captured by XRD, suggesting the layered perovskite crystal structure is not preserved during the reaction. Considering there are only two layers of PbX_4^{2-} octahedra within a free-standing nanoplatelet, any removal of halide ion and B-site exchange would destroy the nanostruc-

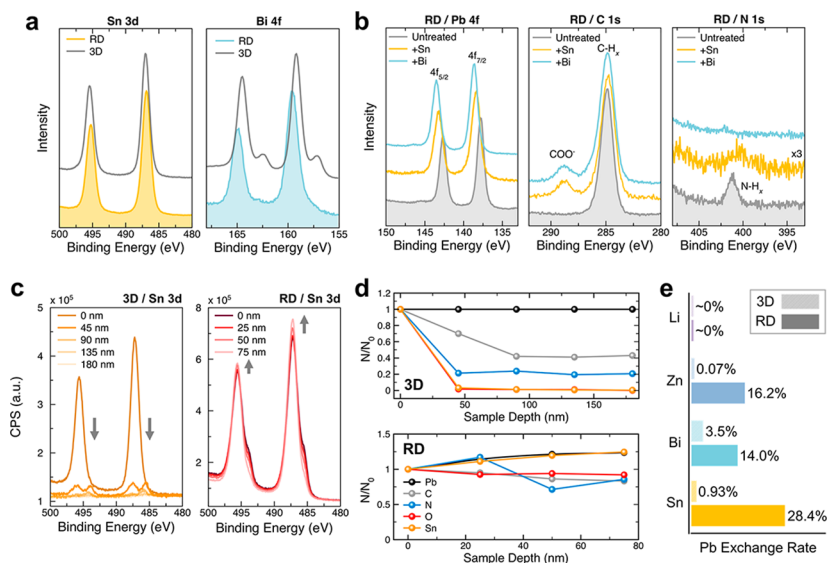


Figure 4. Quantitative compositional characterizations of doped perovskites. (a, b) High-resolution XPS results of (a) tin 3d and bismuth 4f regions and (b) lead 4f, carbon 1s, and nitrogen 1s regions of RD and 3D perovskites before and after dopant treatment. To avoid the Cs 4p feature (~ 159 – 160 eV) obscuring the Bi 4f signals, MA-based RD perovskites (i.e., $(\text{PEA})_2\text{MA}_x\text{Pb}_3\text{Br}_{16-x}$) were used in all XPS studies. (c) XPS depth profile studies of 3D and RD perovskites before and after $\text{Sn}(\text{Oct})_2$ treatment. The film thickness of each sample was confirmed by atomic force microscope measurement. (d) Depth-dependent relative elemental composition of the corresponding 3D and RD perovskites shown in (c); the measured surface atomic concentration of each element is set as 1. The initial drop between 0 and 45 nm in depth in the content of light elements such as carbon, nitrogen, and oxygen may be due to the removal of sample surface contamination. (e) Summary of ICP-OES results of dopant element concentration (atomic percentage) in both types of doped perovskite.

ture and yield amorphous product. The crystallinity difference before and after $\text{Sn}(\text{Oct})_2$ treatment supports the picture that carboxylate ions interact with perovskite surface bulky ammonium cations, remove halide anions, and create vacancies in the perovskite structure, introducing instability within the layered perovskite nanostructures and forming surface trap states that quench the PL of the nanoplatelets, generating instead new trap-induced in-gap emission.

B-Site Doping and Photophysical Studies. Motivated by the fast reaction on nanoplatelets, we further investigated whether the ligand-exchange-driven vacancy creation approach can perform B-site doping on bulk perovskite crystals. We investigate two perovskite classes: $n = 5$ reduced-dimensional (RD) perovskite ($(\text{PEA})_2\text{Cs}_4\text{Pb}_3\text{Br}_{16}$, PEA = phenylethylammonium) and 3D perovskite (MAPbI_3). We also extended dopant candidates to include both isovalent (Sn^{2+} , Zn^{2+}) and heterovalent (Bi^{3+} , Li^+) cations. Both classes of perovskite thin film samples were prepared using the previously established antisolvent approach,^{8,9} followed by an additional soaking step with a chlorobenzene solution containing 0.03 M M_xOct_y , used to assist in the doping process (Experimental Section).

As seen with the nanoplatelets, the reaction between thin film samples and dopant salt is complete within 1 min. It results once again in a significant change in PL behavior. Rapid changes in PL and absorption features were immediately observable after the RD thin film was placed into the dopant solution (Figure 3a and b). The original PL maximum of RD perovskite was at 512 nm and had a narrow PL line width (fwhm = 21 nm, ~ 90 meV). Following exposure to dopant solutions and post-treatment sample purification, the line width of RD perovskite is maintained, and only a slight shift of PL (< 8 nm) is observed, but the PL intensity is notably diminished (Figure 3a). We ascribe this to the formation of surface trap states that create nonradiative recombination pathways. The sharp optical absorption feature is preserved but

the edge is shifted depending on the type of dopant cations (Figure 3b); this may well correlate with the extent of lattice constant change due to doping. Interestingly, the absorption edge at ~ 780 nm remains the same for 3D perovskites' interaction with dopant solutions even after a prolonged reaction time (> 10 min), suggesting that the reactivity of ligand-induced doping is much lower on 3D perovskites (Figure 3c).

We further investigated how dopant cations affect the optoelectronic behavior of RD perovskites by investigating the photophysical properties of RD thin film samples before and after dopant treatment. Compared to nanoplatelet structures, longer PL lifetime decay was observed in RD perovskite thin films ($\tau_{\text{av}} = 13$ ns, Figure 3d). Once the diminished PL intensity was reached following the ligand exchange process, the lifetime decay also experienced a dramatic shortening (τ_{av} values for Sn^{2+} , Bi^{3+} , Zn^{2+} , and Li^+ -doped RD perovskites are 1.1, 0.53, 0.20, and 2.5 ns, respectively). We attribute this to increased defect densities created by the carboxylate/ammonium exchange during the treatment.

To investigate further how the exchange process influences excited-state dynamics in the RD perovskite solid, we performed ultrafast transient absorption spectroscopy to inspect the carrier generation and diffusion processes. The photoexcitation intensity was kept the same for all samples. In the TA spectra (Figure 3e), the ground-state bleach (GSB) peak near the band edge is observed for all the RD perovskites, while no bleach signal is seen in the case of the low- n RD perovskites. We conclude that the RD phase remains stable following dopant incorporation. However, the peak position of the GSB was shifted following the chemical treatment, consistent with band-edge shifting observed in the steady-state absorption spectra. A red-shift of the GSB is observed for Bi^{3+} , Zn^{2+} , and Li^+ -doped RD perovskites. In contrast, for Sn^{2+} -doped RD perovskites, the GSB peak blue-shifts from 504

to 501 nm. The decay of the bleaching signal at the peak wavelength is shown in Figure 3f. Generally, a fast decay process appears at the initial state after pump excitation for each of the doped RD perovskites compared with the case of the control sample, suggesting that new decay channels appear when dopants are introduced. The time constants of the fast decay process for RD perovskites doped with Zn^{2+} , Bi^{3+} , Li^+ , and Sn^{2+} cations are 126, 158, 205, and 342 ps, respectively. We further rule out the possibility of enhanced Auger recombination via the acquisition and analysis of pump-power-dependent TA spectra (Figure S1). The emergence of ultrafast carrier dynamics for the doped perovskite is thus attributed to the defect-related nonradiative recombination introduced by the dopants.

Dopant cations influence the band positions, and the bandgap of perovskites remains a subject of ongoing discussion.^{17,35–37} We therefore combined ultraviolet photoelectron spectroscopy (UPS) with measurements of the optical bandgap (from absorption spectra) to determine the valence band maximum (VBM), work function (WF), and conduction band minimum (CBM) of RD perovskites before and after the doping process (Figures S2 and S3).

The band position is substantially unchanged for the case of exchange with Sn^{2+} and Zn^{2+} , not unexpected since the homovalent dopant shares the same valence as Pb^{2+} . For the exchange with Bi^{3+} , the values of VBM, CBM, and WF increase by 300–450 meV, suggesting that Bi^{3+} -doping produces p-type doped perovskites. No obvious band position change is observed from LiOct-treated RD samples: we conclude that the low solubility of LiOct in chlorobenzene leads to insufficient Li^+ introduction (vide infra, also see Experimental Section for more details).

Quantitative Measurement of Dopant Elements. The photophysical results hint that the dopant elements strongly incorporate into the perovskite RD lattice, whereas doping is limited in the case of the 3D perovskites. We sought to understand differences in the dopant local elemental chemical environment and composition. XPS gave insight into the nature (i.e., composition and oxidation states) of incorporated dopant elements (e.g., Sn^{2+} and Bi^{3+} , Figure 4a). No splitting or broadening of the tin 3d doublet signals is found in a similar binding energy regime (<0.2 eV shift), confirming that the tin cation is present in both Sn-doped RD and 3D perovskites. Characteristic signals for Bi $4f_{5/2}$ (164.9 eV) and $4f_{7/2}$ (159.6 eV) are also found in the Bi-doped RD perovskites, whereas bismuth features shift to a lower energy regime in the 3D perovskite sample (Bi $4f_{5/2}$: 164.6 eV, $4f_{7/2}$: 159.2 eV). In addition, a new doublet Bi signal is found in the lower energy regime (Bi $4f_{5/2}$: 162.6 eV, $4f_{7/2}$: 157.2 eV) attributed to metallic Bi (i.e., Bi^0),³⁸ indicating that the reduction of Bi^{3+} occurs during the doping process. We speculate that this may arise due to the redox reaction between Bi^{3+} and the trace amount of Pb^0 present in 3D perovskites.³⁹

XPS results on lead, carbon, and nitrogen elucidate further the interaction between perovskites and dopant sources (Figure 4b). The doublet signals at 137.7 and 142.6 eV are consistent with Pb^{2+} $4f_{5/2}$ and $4f_{7/2}$, respectively. A shift of the lead features to higher energies occurs in the Sn^{2+} - and Bi^{3+} -doped RD perovskites, while the lead does not shift in the 3D perovskites (Figure S4). This may be due to stronger Pb–X interaction in doped RD perovskites caused by impurity cation incorporation.^{18,40} In addition, after treatment of the RD perovskites, the N– H_x signal disappears from the nitrogen 1s

spectrum, and a new 288.9 eV signal emerges in the carbon 1s spectrum. In contrast, neither the energy shift of the lead nor the presence of new COO^- signals is found in the 3D counterparts (Figure S4). We conclude that only RD perovskites enable the insertion of the dopant cation into the crystal lattice and efficient ammonium/carboxylate ligand exchange, whereas 3D perovskites are substantially inert in the context of the doping process.

We also performed depth-profile studies of Sn-doped 3D and RD perovskites (Figure 4c). The samples were sputtered to the desired depth to obtain subsurface elemental information. The strong Sn 3d doublet at 495.6 eV (Sn $3d_{3/2}$) and 487.1 eV (Sn $3d_{5/2}$) is seen at the surface (i.e., 0 nm depth) of each class of samples. These Sn binding energies are higher than the reported value of Sn^{2+} in Sn–Pb perovskite thin films,⁴¹ indicating that the exchanged surface Sn^{2+} has been fully oxidized prior to XPS measurement. As the sputtering depth increases within the 3D perovskite, a significant signal intensity decrease is observed, accompanied by the presence of the pristine, nonoxidized Sn^{2+} doublet signals at slightly lower binding energies (493.9 eV (Sn $3d_{3/2}$) and 485.5 eV (Sn $3d_{5/2}$)).

The RD perovskite, in contrast, shows a uniform distribution of tin in the thin film (Figure 4c). The depth-dependent atomic concentrations of the major elements present in doped 3D and RD perovskites are summarized in Figure 4d. All elements present at the surface of $\text{Sn}(\text{Oct})_2$ -treated RD perovskites maintain similar concentrations throughout the entire sample. Specifically, the consistent amount of oxygen suggests the carboxylate/ammonium ligand exchange occurs throughout the entire RD crystal structure. As for the 3D counterpart, while the concentration of lead is not independent of the sputtering depth, the other major elements including tin show a significant drop in concentration. Comparing the depth-dependent concentration change of tin, we conclude that the ligand-exchange-assisted B-site exchange is successful in the entire depth of the RD perovskite structure, whereas in the 3D perovskite, only the surface atoms are exchanged.

We next acquired the elemental composition of doped perovskites using ICP-OES (Figures 4e and S5–S7, Table S1). An extremely low concentration of the dopant element was found in all treated 3D perovskites, consistent with XPS analyses discussed above. As for RD perovskites, up to 28% and 16% of Pb^{2+} can be exchanged to Sn^{2+} and Zn^{2+} . The exchange is also very efficient for heterovalent cations: 14% of Bi was confirmed incorporated into RD perovskites, ~40 times higher than the previously reported *in situ* and postsynthetic Bi^{3+} doping process on all perovskite solids.¹⁷ It should be noted that the doping level of Li^+ is also low for RD perovskites, which may be due to the extremely low solubility of $\text{Li}(\text{Oct})_2$ in chlorobenzene (Experimental Section). The significantly weakened PL of the LiOct-treated RD samples (Figure 3a) is consistent with the view that the PL quench originates from the interaction between the perovskite and the carboxylate.

Crystal Structure Characterization. We investigated the impact of B-site doping on crystal structure using X-ray-based characterization. PXRD results confirm that the crystallinity of the 3D perovskite pattern is not changed following dopant treatments (Figure S8). As for RD perovskites, while most crystal peak positions are retained, the intensity change of certain specific peaks (e.g., (002), (006)) is evident following dopant treatment (Figures 5a and S9), suggesting changes in

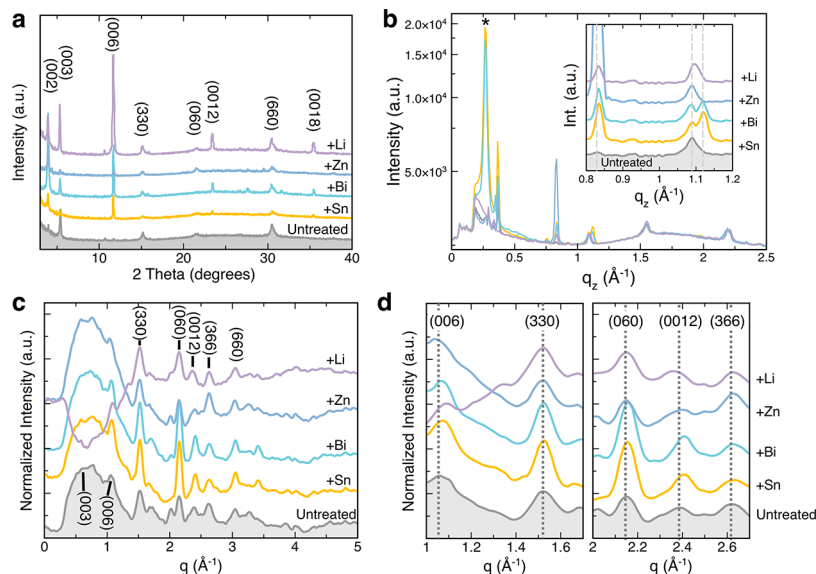


Figure 5. Structural analyses of doped perovskites. (a) PXRD patterns of pristine and doped RD perovskites. (b) Cuts along the q_z axis of experimental GIWAXS measurements on pristine and doped RD perovskites. Signals originating from an incompletely blocked incident beam are denoted using an asterisk (*). The inset shows the diffraction patterns in the range of 0.8–1.2 \AA^{-1} , clearly showing the peak shift and emergence of new signals after dopant treatment. Dotted lines indicate the q values corresponding to peak maxima of the pattern of untreated RD sample. (c) High-energy X-ray diffraction patterns of pristine and doped RD perovskites. (d) Diffraction patterns corresponding to (c) in the ranges of 1.0–1.7 and 2.0–2.7 \AA^{-1} . Dotted lines in (b) inset and (d) indicate the q values corresponding to peak maxima of the pattern of untreated RD sample.

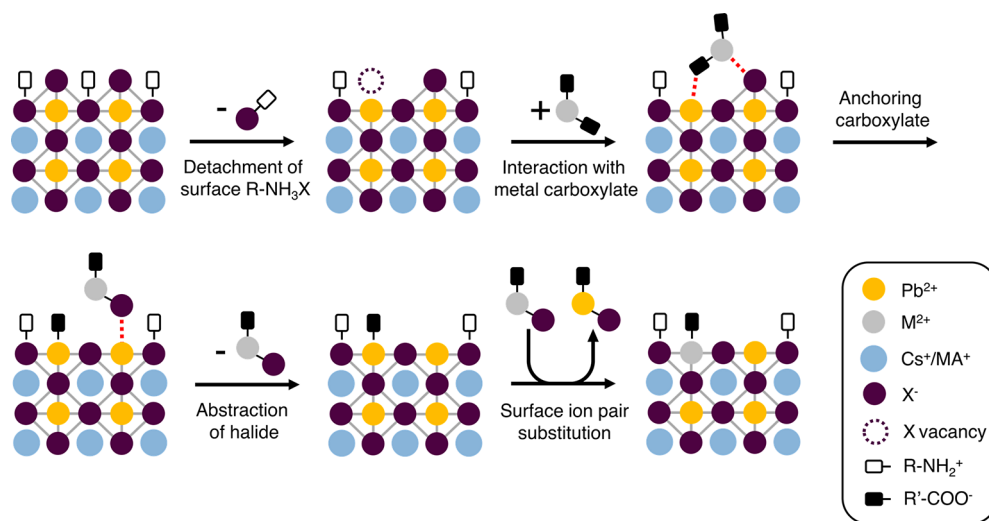


Figure 6. Schematic illustration of the ligand-assisted B-site cation exchange mechanism. The process was initiated by the dynamic detachment of the bulky organic anion–cation pair due to the intrinsic perovskite features (ionic surface and liquid-like crystal structures) and the interaction with dopant ion pair. The removal of the halide enables the anchoring of carboxylate on surface Pb^{2+} and enables the dopant intermediate (metal halide carboxylate) to abstract the adjacent halide. The B-site exchange then proceeds by the substitution of surface ion pair $\text{Pb}-\text{Oct}$ with dopant ion pair $\text{M}-\text{Oct}$, yielding a dopant-anchored surface.

the orientation of crystal grain domains upon doping. Interestingly, although Li^+ does not successfully incorporate into RD perovskite, LiOct -treated RD perovskite exhibits an evident peak intensity change. This suggests the carboxylic/ammonium ligand exchange itself may influence strongly the crystal domain orientation change.

In order to capture the signals distinguishing the perovskite crystal orientations, GIWAXS measurements (Figures 5b and Supplementary Figures S10–S12) were used to reveal the orientation of quantum wells within these two types of perovskites. The isotropic ring pattern in 3D perovskite films evidences bulk MAPbI_3 crystal grains with no preferential

growth orientation (Figure S10), whereas the majority of signals of RD films along the q_z axis suggests that the perovskite layers ($n = 5$) preferentially orient parallel to the substrate (Figure S11), in good agreement with the previous studies.¹¹ No observable change in GIWAXS features was seen from 3D perovskites before and after dopant treatment (Figure S10). In the RD case, although no appreciable difference in the diffraction pattern is found before vs after dopant treatment, we did observe a small shift (0.002–0.004 \AA^{-1}) in peak positions along the q_z and q_{xy} axes in the case of doped RD samples (Figure S11), accompanied by the emergence of new crystal signals at 0.5 and 1.12 \AA^{-1} (Figure S12). XRD and

GIWAXS results indicate that the ligand-assisted B-site doping process does not affect the crystal structures of RD perovskites, while it only introduces shrinkage of crystal unit cells due to the smaller ionic radii of dopant elements.

We therefore used high-resolution XRD to further investigate crystal strain within the perovskite solid introduced by B-site doping. The position and intensity of major crystal peaks were substantially maintained in 3D and RD perovskites following treatment (Figures 5c and S13); yet peak shifts to slightly larger q values were also found in RD crystal orientations parallel to the substrate, such as (003), (006), and (0012). These observations are in excellent agreement with PXRD and GIWAXS results, and together these findings suggest that the ligand-exchange-assisted B-site exchange leads to an asymmetric lattice contraction of the RD perovskite mainly in the (001) direction (i.e., along the layering direction).

The materials investigations presented above lead us to a more detailed model of the ligand-exchange-assisted doping process (Figure 6). While the activation energy is high for B-site vacancy creation, the presence of the bulky organic A-site enables an indirect approach to B-site doping. The process is initiated by the dynamic detachment of anion–cation pair $R-NH_3X$ (where R is the bulky organic component) facilitated by the ionic surface and liquid-like crystal structure and the opportunity to interact with metal carboxylate. Because 3D perovskite does not have bulky organic cations (R), the exchange rate of carboxylate/methylammonium (i.e., MA^+) is impeded in the 3D case, and only the potential carboxylic/ MA^+ exchange is available, yielding carboxylate-passivated surfaces.

The removal of the halide X^- opens the PbX_4^{2-} octahedron, enabling Pb^{2+} to interact with the dopant molecule and become bonded by carboxylate. It is important to note that the adjacent X^- can now interact with the dopant ion pair, after which it is poised to and then detach from the surface. Due to the nature of the dynamic surface, surface ion pair $Pb-Oct$ then is capable of being exchanged by the dopant ion pair and forming a dopant-anchored surface. The ongoing doping process, followed by cation diffusion within the perovskite solid, is then able to proceed, with additional dopant cations fed in from the surface and traveling for incorporation deeper into the lattice,^{22,26} resulting in homogeneously doped RD perovskites.

4. CONCLUSIONS

We report a general perovskite doping approach that replaces Pb^{2+} with desired B-site cations under mild conditions. The highest level of heterovalent doping is 14% for reduced-dimensional perovskite films, 40 times higher than in previously reported postsynthesis doping on perovskite solids. We achieved this via a surface-ligand-exchange-inspired dynamic ion exchange process that substantially reduces the activation energy of B-site vacancy formation at the boundary of RD perovskite flakes. The anchoring of the dopant substantially modifies the optoelectronic properties of perovskites without additional damage nor reconstruction of the crystal, a finding that may have applications in doped transport layers for light-emitting diodes. This work demonstrated that the strategy can be extended to the application of perovskite nanomaterial doping and 3D perovskite surface passivation and provides an approach that can be further combined with scaled solution-based processing techniques such as spray-coating, blade coating, and roll-to-roll printing.

■ ASSOCIATED CONTENT

Supporting Information

The Supporting Information is available free of charge on the ACS Publications website at DOI: 10.1021/jacs.9b02565.

UPS and bandgap alignment of doped and undoped RD perovskite thin films; additional XPS and XRD results of doped and undoped 3D perovskite thin films; summary of ICP-OES results of doped and undoped perovskite thin films and corresponding calibration curves; additional GIWAXS and high-energy XRD results of doped and undoped perovskite thin films (PDF)

■ AUTHOR INFORMATION

Corresponding Author

*ted.sargent@utoronto.ca

ORCID

Zhenyu Yang: 0000-0002-6403-8679

Oleksandr Voznyy: 0000-0002-8656-5074

Mengxia Liu: 0000-0002-1676-705X

Rafael Quintero-Bermudez: 0000-0002-4233-395X

James Z. Fan: 0000-0002-1594-865X

Li Na Quan: 0000-0001-9301-3764

Grant Walters: 0000-0002-9005-2335

U-Ser Jeng: 0000-0002-2247-5061

Shana O. Kelley: 0000-0003-3360-5359

Edward H. Sargent: 0000-0003-0396-6495

Present Address

[¶]School of Chemistry, Sun Yat-Sen University, Guangzhou, People's Republic of China, 510275.

Author Contributions

[#]Z.Y. and M.W. contributed equally.

Notes

The authors declare no competing financial interest.

■ ACKNOWLEDGMENTS

This publication is based in part on work supported by the Ontario Research Fund - Research Excellence Program, by the Natural Sciences and Engineering Research Council of Canada (NSERC), and by the US Department of the Navy, Office of Naval Research (Grant Award No.: N00014-17-1-2524). H.T. acknowledges The Netherlands Organisation for Scientific Research (NWO) for a Rubicon grant (680-50-1511) to support his postdoctoral research at University of Toronto. The authors thank Mr. P. Li and Prof. Z. H. Lu (MSE, University of Toronto) for UPS measurement and analysis. Dr. D. S. Robinson (Argonne National Laboratory) is thanked for the assistance with high-energy XRD measurements. Mr. C.-Y. Lin (CE, National Tsing Hua University) and Dr. C. S. Tan (ECE, University of Toronto) are thanked for the assistance with GIWAXS measurements. Dr. Y. Wang (University of Toronto) is thanked for the figure design and optimization. Mr. R. Wolowiec, Mr. D. Kopilovic, and Ms. E. Palmiano (University of Toronto) are thanked for their help in laboratory maintenance.

■ REFERENCES

(1) Li, Z.; Klein, T. R.; Kim, D. H.; Yang, M.; Berry, J. J.; van Hest, M. F. A. M.; Zhu, K. Scalable fabrication of perovskite solar cells. *Nature Reviews Materials* **2018**, *3*, 18017.

- (2) Kagan, C. R.; Mitzi, D. B.; Dimitrakopoulos, C. D. Organic-Inorganic Hybrid Materials as Semiconducting Channels in Thin-Film Field-Effect Transistors. *Science* **1999**, *286* (5441), 945.
- (3) Tan, Z.-K.; Moghaddam, R. S.; Lai, M. L.; Docampo, P.; Higler, R.; Deschler, F.; Price, M.; Sadhanala, A.; Pazos, L. M.; Credgington, D.; Hanusch, F.; Bein, T.; Snaith, H. J.; Friend, R. H. Bright light-emitting diodes based on organometal halide perovskite. *Nat. Nanotechnol.* **2014**, *9*, 687.
- (4) Yakunin, S.; Dirin, D. N.; Shynkarenko, Y.; Morad, V.; Cherniukh, I.; Nazarenko, O.; Kreil, D.; Nauser, T.; Kovalenko, M. V. Detection of gamma photons using solution-grown single crystals of hybrid lead halide perovskites. *Nat. Photonics* **2016**, *10*, 585.
- (5) Zhang, R.; Fan, J.; Zhang, X.; Yu, H.; Zhang, H.; Mai, Y.; Xu, T.; Wang, J.; Snaith, H. J. Nonlinear Optical Response of Organic-Inorganic Halide Perovskites. *ACS Photonics* **2016**, *3* (3), 371–377.
- (6) Luo, J.; Im, J.-H.; Mayer, M. T.; Schreier, M.; Nazeeruddin, M. K.; Park, N.-G.; Tilley, S. D.; Fan, H. J.; Grätzel, M. Water photolysis at 12.3% efficiency via perovskite photovoltaics and Earth-abundant catalysts. *Science* **2014**, *345* (6204), 1593.
- (7) Peng, X. Mechanisms for the Shape-Control and Shape-Evolution of Colloidal Semiconductor Nanocrystals. *Adv. Mater.* **2003**, *15* (5), 459–463.
- (8) Yang, W. S.; Noh, J. H.; Jeon, N. J.; Kim, Y. C.; Ryu, S.; Seo, J.; Seok, S. I. High-performance photovoltaic perovskite layers fabricated through intramolecular exchange. *Science* **2015**, *348* (6240), 1234–1237.
- (9) Yuan, M.; Quan, L. N.; Comin, R.; Walters, G.; Sabatini, R.; Voznyy, O.; Hoogland, S.; Zhao, Y.; Beauregard, E. M.; Kanjanaboos, P.; Lu, Z.; Kim, D. H.; Sargent, E. H. Perovskite energy funnels for efficient light-emitting diodes. *Nat. Nanotechnol.* **2016**, *11*, 872.
- (10) Wang, N.; Cheng, L.; Ge, R.; Zhang, S.; Miao, Y.; Zou, W.; Yi, C.; Sun, Y.; Cao, Y.; Yang, R.; Wei, Y.; Guo, Q.; Ke, Y.; Yu, M.; Jin, Y.; Liu, Y.; Ding, Q.; Di, D.; Yang, L.; Xing, G.; Tian, H.; Jin, C.; Gao, F.; Friend, R. H.; Wang, J.; Huang, W. Perovskite light-emitting diodes based on solution-processed self-organized multiple quantum wells. *Nat. Photonics* **2016**, *10*, 699.
- (11) Cao, D. H.; Stoumpos, C. C.; Farha, O. K.; Hupp, J. T.; Kanatzidis, M. G. 2D Homologous Perovskites as Light-Absorbing Materials for Solar Cell Applications. *J. Am. Chem. Soc.* **2015**, *137* (24), 7843–7850.
- (12) Grancini, G.; Roldán-Carmona, C.; Zimmermann, I.; Mosconi, E.; Lee, X.; Martineau, D.; Nabey, S.; Oswald, F.; De Angelis, F.; Graetzel, M.; Nazeeruddin, M. K. One-Year stable perovskite solar cells by 2D/3D interface engineering. *Nat. Commun.* **2017**, *8*, 15684.
- (13) Kieslich, G.; Sun, S.; Cheetham, A. K. An extended Tolerance Factor approach for organic-inorganic perovskites. *Chemical Science* **2015**, *6* (6), 3430–3433.
- (14) Noh, J. H.; Im, S. H.; Heo, J. H.; Mandal, T. N.; Seok, S. I. Chemical Management for Colorful, Efficient, and Stable Inorganic–Organic Hybrid Nanostructured Solar Cells. *Nano Lett.* **2013**, *13* (4), 1764–1769.
- (15) Saliba, M.; Matsui, T.; Domanski, K.; Seo, J.-Y.; Ummadisingu, A.; Zakeeruddin, S. M.; Correa-Baena, J.-P.; Tress, W. R.; Abate, A.; Hagfeldt, A.; Grätzel, M. Incorporation of rubidium cations into perovskite solar cells improves photovoltaic performance. *Science* **2016**, *354* (6309), 206–209.
- (16) Zhou, Y.; Chen, J.; Bakr, O. M.; Sun, H.-T. Metal-Doped Lead Halide Perovskites: Synthesis, Properties, and Optoelectronic Applications. *Chem. Mater.* **2018**, *30* (19), 6589–6613.
- (17) Abdelhady, A. L.; Saidaminov, M. I.; Murali, B.; Adinolfi, V.; Voznyy, O.; Katsiev, K.; Alarousu, E.; Comin, R.; Dursun, I.; Sinatra, L.; Sargent, E. H.; Mohammed, O. F.; Bakr, O. M. Heterovalent Dopant Incorporation for Bandgap and Type Engineering of Perovskite Crystals. *J. Phys. Chem. Lett.* **2016**, *7* (2), 295–301.
- (18) Zhang, J.; Shang, M.-h.; Wang, P.; Huang, X.; Xu, J.; Hu, Z.; Zhu, Y.; Han, L. n-Type Doping and Energy States Tuning in CH₃NH₃Pb_{1-x}Sb_{2x/3} Perovskite Solar Cells. *ACS Energy Letters* **2016**, *1* (3), 535–541.
- (19) Ma, J.-P.; Chen, Y.-M.; Zhang, L.-M.; Guo, S.-Q.; Liu, J.-D.; Li, H.; Ye, B.-J.; Li, Z.-Y.; Zhou, Y.; Zhang, B.-B.; Bakr, O. M.; Zhang, J.-Y.; Sun, H.-T. Insights into the local structure of dopants, doping efficiency, and luminescence properties of lanthanide-doped CsPbCl₃ perovskite nanocrystals. *J. Mater. Chem. C* **2019**, *7* (10), 3037–3048.
- (20) Stoumpos, C. C.; Malliakas, C. D.; Kanatzidis, M. G. Semiconducting Tin and Lead Iodide Perovskites with Organic Cations: Phase Transitions, High Mobilities, and Near-Infrared Photoluminescent Properties. *Inorg. Chem.* **2013**, *52* (15), 9019–9038.
- (21) Liu, W.; Lin, Q.; Li, H.; Wu, K.; Robel, I.; Pietryga, J. M.; Klimov, V. I. Mn²⁺-Doped Lead Halide Perovskite Nanocrystals with Dual-Color Emission Controlled by Halide Content. *J. Am. Chem. Soc.* **2016**, *138* (45), 14954–14961.
- (22) Akkerman, Q. A.; Rainò, G.; Kovalenko, M. V.; Manna, L. Genesis, challenges and opportunities for colloidal lead halide perovskite nanocrystals. *Nat. Mater.* **2018**, *17* (5), 394–405.
- (23) deQuilettes, D. W.; Zhang, W.; Burlakov, V. M.; Graham, D. J.; Leijtens, T.; Oshero, A.; Bulović, V.; Snaith, H. J.; Ginger, D. S.; Stranks, S. D. Photo-induced halide redistribution in organic-inorganic perovskite films. *Nat. Commun.* **2016**, *7*, 11683.
- (24) Yuan, Y.; Huang, J. Ion Migration in Organometal Trihalide Perovskite and Its Impact on Photovoltaic Efficiency and Stability. *Acc. Chem. Res.* **2016**, *49* (2), 286–293.
- (25) Eperon, G. E.; Ginger, D. S. B-Site Metal Cation Exchange in Halide Perovskites. *ACS Energy Letters* **2017**, *2* (5), 1190–1196.
- (26) van der Stam, W.; Geuchies, J. J.; Altantzis, T.; van den Bos, K. H. W.; Meeldijk, J. D.; Van Aert, S.; Bals, S.; Vanmaekelbergh, D.; de Mello Donega, C. Highly Emissive Divalent-Ion-Doped Colloidal CsPb_{1-x}MxBr₃ Perovskite Nanocrystals through Cation Exchange. *J. Am. Chem. Soc.* **2017**, *139* (11), 4087–4097.
- (27) Li, F.; Xia, Z.; Gong, Y.; Gu, L.; Liu, Q. Optical properties of Mn²⁺ doped cesium lead halide perovskite nanocrystals via a cation-anion co-substitution exchange reaction. *J. Mater. Chem. C* **2017**, *5* (36), 9281–9287.
- (28) Boles, M. A.; Ling, D.; Hyeon, T.; Talapin, D. V. The surface science of nanocrystals. *Nat. Mater.* **2016**, *15*, 141.
- (29) Sichert, J. A.; Tong, Y.; Mutz, N.; Vollmer, M.; Fischer, S.; Milowska, K. Z.; García Cortadella, R.; Nickel, B.; Cardenas-Daw, C.; Stolarczyk, J. K.; Urban, A. S.; Feldmann, J. Quantum Size Effect in Organometal Halide Perovskite Nanoplatelets. *Nano Lett.* **2015**, *15* (10), 6521–6527.
- (30) Weidman, M. C.; Seitz, M.; Stranks, S. D.; Tisdale, W. A. Highly Tunable Colloidal Perovskite Nanoplatelets through Variable Cation, Metal, and Halide Composition. *ACS Nano* **2016**, *10* (8), 7830–7839.
- (31) Chia, H.-C.; Sheu, H.-S.; Hsiao, Y.-Y.; Li, S.-S.; Lan, Y.-K.; Lin, C.-Y.; Chang, J.-W.; Kuo, Y.-C.; Chen, C.-H.; Weng, S.-C.; Su, C.-J.; Su, A.-C.; Chen, C.-W.; Jeng, U. S. Critical Intermediate Structure That Directs the Crystalline Texture and Surface Morphology of Organo-Lead Trihalide Perovskite. *ACS Appl. Mater. Interfaces* **2017**, *9* (42), 36897–36906.
- (32) Eames, C.; Frost, J. M.; Barnes, P. R. F.; O'Regan, B. C.; Walsh, A.; Islam, M. S. Ionic transport in hybrid lead iodide perovskite solar cells. *Nat. Commun.* **2015**, *6*, 7497.
- (33) Li, M.; Zhang, X.; Matras-Postolek, K.; Chen, H.-S.; Yang, P. An anion-driven Sn²⁺ exchange reaction in CsPbBr₃ nanocrystals towards tunable and high photoluminescence. *J. Mater. Chem. C* **2018**, *6* (20), 5506–5513.
- (34) Jun, P.; Na, Q. L.; Yongbiao, Z.; Wei, P.; Banavoth, M.; P, S. S.; Mingjian, Y.; Lutfan, S.; M, A. N.; Jiakai, L.; Emre, Y.; Zhenyu, Y.; Oleksandr, V.; Riccardo, C.; N, H. M.; F, M. O.; Hong, L. Z.; Ha, K. D.; H, S. E.; M, B. O. Highly Efficient Perovskite-Quantum-Dot Light-Emitting Diodes by Surface Engineering. *Adv. Mater.* **2016**, *28* (39), 8718–8725.
- (35) Zhang, Z.; Ren, L.; Yan, H.; Guo, S.; Wang, S.; Wang, M.; Jin, K. Bandgap Narrowing in Bi-Doped CH₃NH₃PbCl₃ Perovskite Single Crystals and Thin Films. *J. Phys. Chem. C* **2017**, *121* (32), 17436–17441.

(36) Nayak, P. K.; Sendner, M.; Wenger, B.; Wang, Z.; Sharma, K.; Ramadan, A. J.; Lovrinčić, R.; Pucci, A.; Madhu, P. K.; Snaith, H. J. Impact of Bi³⁺ Heterovalent Doping in Organic–Inorganic Metal Halide Perovskite Crystals. *J. Am. Chem. Soc.* **2018**, *140* (2), 574–577.

(37) Lozhkina, O. A.; Murashkina, A. A.; Shilovskikh, V. V.; Kapitonov, Y. V.; Ryabchuk, V. K.; Emeline, A. V.; Miyasaka, T. Invalidity of Band-Gap Engineering Concept for Bi³⁺ Heterovalent Doping in CsPbBr₃ Halide Perovskite. *J. Phys. Chem. Lett.* **2018**, *9* (18), 5408–5411.

(38) Hu, Y.; Qiu, T.; Bai, F.; Miao, X.; Zhang, S. Enhancing moisture-tolerance and photovoltaic performances of FAPbI₃ by bismuth incorporation. *J. Mater. Chem. A* **2017**, *5* (48), 25258–25265.

(39) Miller, E. M.; Zhao, Y.; Mercado, C. C.; Saha, S. K.; Luther, J. M.; Zhu, K.; Stevanović, V.; Perkins, C. L.; van de Lagemaat, J. Substrate-controlled band positions in CH₃NH₃PbI₃ perovskite films. *Phys. Chem. Chem. Phys.* **2014**, *16* (40), 22122–22130.

(40) Navas, J.; Sánchez-Coronilla, A.; Gallardo, J. J.; Martín, E. I.; Hernández, N. C.; Alcántara, R.; Fernández-Lorenzo, C.; Martín-Calleja, J. Revealing the role of Pb²⁺ in the stability of organic–inorganic hybrid perovskite CH₃NH₃Pb_{1-x}CdxI₃: an experimental and theoretical study. *Phys. Chem. Chem. Phys.* **2015**, *17* (37), 23886–23896.

(41) Ito, N.; Kamarudin, M. A.; Hirotsu, D.; Zhang, Y.; Shen, Q.; Ogomi, Y.; Iikubo, S.; Minemoto, T.; Yoshino, K.; Hayase, S. Mixed Sn–Ge Perovskite for Enhanced Perovskite Solar Cell Performance in Air. *J. Phys. Chem. Lett.* **2018**, *9* (7), 1682–1688.